New insights in structural characterization of transparent ZnS ceramics hot-pressed from nanocrystalline powders synthesized by combustion method

G.R. Durand, Noha Hakmeh, V. Dorcet, Valérie Demange, François Cheviré, O. Merdrignac-Conanec

To cite this version:

G.R. Durand, Noha Hakmeh, V. Dorcet, Valérie Demange, François Cheviré, et al.. New insights in structural characterization of transparent ZnS ceramics hot-pressed from nanocrystalline powders synthesized by combustion method. Journal of the European Ceramic Society, 2019, 39 (10), pp.3094-3102. 10.1016/j.jeurceramsoc.2019.03.033 . hal-02122177

HAL Id: hal-02122177
https://univ-rennes.hal.science/hal-02122177

New insights in structural characterization of transparent ZnS ceramics hot-pressed from nanocrystalline powders synthesized by combustion

Guillaume R.G. Durand[1], Noha Hakmeh[1], Vincent Dorcet[2], Valérie Demange[2],
François Cheviré[1], Odile Merdrignac-Conanec[1]*

[1]Univ Rennes, CNRS, ISCR (Institut des Sciences Chimiques de Rennes) - UMR 6226, F-35000 RENNES, France
[2]Univ Rennes, CNRS, ISCR – UMR 6226, ScanMAT – UMS 2001, F-35000 RENNES, France

*Corresponding author:
Dr. Odile Merdrignac-Conanec
Institut des Sciences Chimiques de Rennes, UMR CNRS 6226
Université de Rennes 1, Campus de Beaulieu
35042 Rennes Cedex, France
E-mail address: odile.merdrignac@univ-rennes1.fr

1. Abstract

Zinc sulfide transparent ceramics have been fabricated by hot pressing (HP) powders prepared by a newly developed combustion method. Chemical, structural and microstructural properties of powders and ceramics were characterized using different experimental techniques (XRD, SEM-EDS, laser granulometry, TEM, BET, FT-IR spectroscopy). ZnS powders were densified to full density by HP under vacuum atmosphere. The ceramics exhibit highly dense microstructure with mean grain size of 1 µm. TEM characterization identified, both in powders and ceramics, twins and simple stacking faults due to the aperiodic distribution of hexagonal domains. With optical transmission of the theoretical level (~75%), without absorption band (at 6 µm) and with negligible optical loss, in the 4-12 µm region, the ceramics exhibit better optical performances than standard grade CVD ZnS, and unprecedented performances for hot-pressed ZnS.

2. Introduction

Polycrystalline zinc sulfide (ZnS) is a reference material for optical applications as infrared window and dome materials. Its cubic structure and wide band-gap (3.68 eV) make its optical transmission rather unique, ranging from the visible to the long wave infrared region (0.4 µm-12 µm) [1–3]. In addition, its thermo-mechanical performances surpass those of its competitors, germanium and zinc selenide, so that ZnS is the preferred choice for military applications or other harsh environments. Various elaboration techniques have been already studied for producing ZnS optics or windows such as Chemical Vapor Deposition (CVD) [4–8], Hot Pressing (HP) [9–20] or, more recently, Field Assisted Sintering Technique (FAST or SPS) [21–24]. CVD is, by far, the most important process and produces standard grade CVD ZnS also called FLIR grade. CVD ZnS has a color ranging from dark yellow to red, is a poor visible transmitter and presents an absorption at about 6 µm, attributed to Zn-H species, particular to the CVD deposition process. Post-deposition Hot Isostatic Pressing (HIP) converts standard grade ZnS into transparent, colorless ZnS, also called Cleartran® or Multispectral® exhibiting a higher transmission level in the visible range [25]. However, CVD and HIP are long and complex processes so that ZnS products are currently available at a very high cost and applied almost exclusively for the military industry [5–7]. Furthermore, CVD-HIP processes produce coarse ceramics with poor mechanical properties due to recrystallization and grain growth [26–29]. Research on sintering techniques (HP or FAST) as alternatives to CVD has thus gained much interest in the last decade considering the numerous advantages they offer as near-net shaping, large-scale production, reduced manufacturing costs and especially enhanced mechanical durability when applied with sub-micrometric or nanometric powders [12–24].

In this study, high purity ZnS nanopowders were synthesized via a newly developed combustion method and further densified by HP under vacuum in an attempt to produce transparent ZnS ceramics with optical performances superior to that of standard grade CVD ZnS. Physico-chemical and microstructural characteristics of powders and ceramics have been reported and discussed in close correlation with the optical properties.

3. Experimental procedure

ZnS powders were obtained following a novel patented solution combustion method followed by a sulfurization step [16,30]. Zinc nitrate hexahydrate $Zn(NO_3)_2$, $6H_2O$ (Alfa Aesar, 99,998%) and thioacetamide (TAA) CH_3CSNH_2 (Sigma Aldrich, ≥ 99%, ACS Reagent) were used as starting materials. As-combusted powders were subsequently heat-treated in pure H_2S flow in a tubular furnace at 600°C for 2 h. Next, pure ZnS powders were densified by Hot Pressing (HP) under vacuum (about 10^{-1} mbar) at 950°C to prevent the critical cubic sphalerite/hexagonal wurtzite phase transition occuring at 1020°C. A typical quantity of 4 g of ZnS powder was introduced in a 20 mm diameter graphite die. Heating rate was 10°C/min and 120 MPa was applied at the sintering temperature for dwell times of 2, 4 and 6 h. After hot-pressing, the samples were optically polished with a final step using 0.5 µm alumina powder.

X-Ray Diffraction (XRD) patterns were collected at room temperature in the 2θ range 5-90° with a step size of 0.026° and a scan time per step of 40 s using a PANalytical X'Pert Pro diffractometer (Cu K-L2,L3 radiation, 40 kV, 40 mA, PIXcel 1D detector). Data Collector and High-Score Plus softwares were used, respectively, for recording and analysis of the patterns. ZnS hexagonal fraction was determined by a calculation method proposed by Bansagi *et al.*[31] and Xue and Raj [32].

Fourier Transform Infra-Red (FTIR) spectroscopy was carried out with a Nicolet 380 FT-IR spectrometer (Thermo Electron Corporation) in the 400-4000 cm^{-1} range. Powder samples were pelleted after careful grinding with anhydrous KBr (99+%, FT-IR grade, Sigma-Aldrich) and compared with freshly prepared blank KBr pellets. Infrared transmission spectra of the ceramics were performed in the 2.5-16 µm range on polished samples of 1.5 mm thick. The calculation of the theoretical transmission maximum for cubic ZnS based on its refractive index variation (at room temperature), from 2.26 at 2.5 µm to 2.13 at 14 µm, gives a value of 75% [33].

A FlowSorb II 2300 Micromeritics apparatus was used to determine the Specific Surface Area (SSA) of the powders by the Brunauer-Emmett-Teller single point method. Before measurement, the samples were outgassed under N_2/He flow at 250°C for 30 min.

Laser granulometry measurements were performed with a CILAS 1180 particle size analyzer. Powders were dispersed in water using sodium hexametaphosphate as dispersing agent and were exposed to ultrasounds during analysis.

Powders morphology and ceramics microstructure were examined by Scanning Electron Microscopy (SEM) with a JEOL JSM IT300 equipment (CMEBA, university of Rennes 1) and Transmission Electron Microscopy (TEM) with a JEOL 2100 operating at 200 kV (THEMIS, university of Rennes 1). Prior to SEM observations, the samples were metallized with Au-Pd. The chemical composition of the powder samples was analyzed by Energy Dispersive Spectroscopy (EDS, Oxford Aztec), attached to the SEM, on samples metallized with amorphous carbon. Grain boundaries of hot-pressed polished ceramics were revealed by thermal etching at 900°C for 30 min in $H_2S(10\%)/N_2$ flow to prevent the samples from oxidation. Grain size distributions were determined from about 300 to 400 grains via the ImageJ software. For TEM, powder samples were crushed in a mortar in presence of ethanol, while ceramic samples were pre-thinned with the help of a Fischione dimpler and thinned with a Fischione Ion Milling instrument (Model 1010).

The apparent density of the sintered samples was measured by the immersion method in absolute ethanol. The precision of this measurement technique is of about 1%. The relative density of the ceramics was calculated using a theoretical density of 4.08 $g.cm^{-3}$ (ZnS, JCPDS 96-110-1051).

4. Results

4.1. Powders synthesis and characterization

Fig. 1 presents the XRD patterns of the powders before and after heat-treatment in H_2S. Pattern analysis of the as-combusted (raw) powder points out cubic zinc sulfide (JCPDS 96-110-1051) as the major phase and zinc oxide ZnO and zinc oxysulfate $Zn_3O(SO_4)_2$ as minor phases. XRD analysis confirms that H_2S heat-treatment leads to pure ZnS powders. The latter consist, predominantly, in cubic sphalerite ZnS with a proportion of about 10 to 20% of hexagonal wurtzite phase.

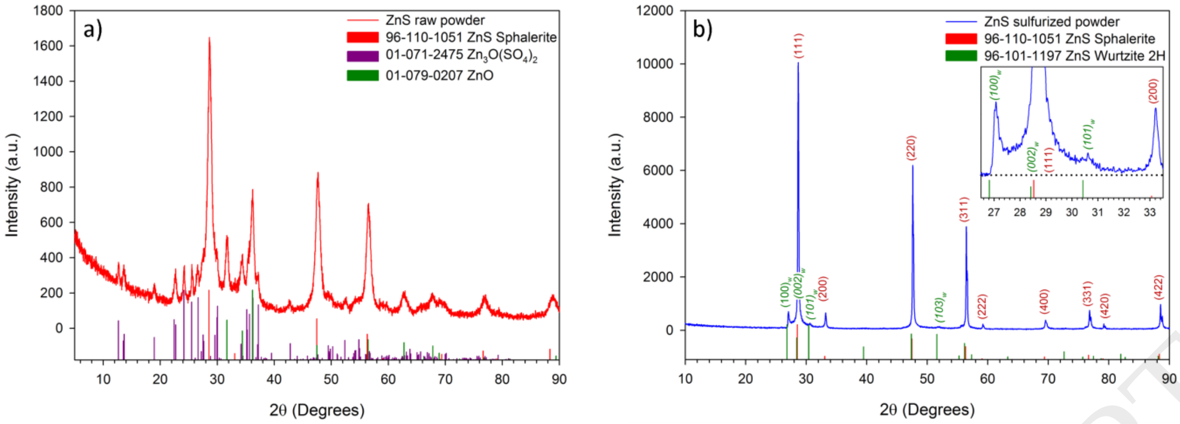

Fig. 1. X-ray diffraction patterns of a) as-combusted (raw) b) sulfurized ZnS powder

The FTIR spectra of raw and sulfurized powders are compared in Fig. 2. Raw powders show strong absorption bands at 3000-3600 cm^{-1} and 1640 cm^{-1}, that are characteristic of stretching and bending modes of the H_2O molecules respectively [34–36]. The strong absorption bands at 1000-1200 cm^{-1} and the weak absorption band between 600 and 650 cm^{-1} are assigned to the stretching and the bending modes of sulfate species respectively [37,38]. The band at 450 cm^{-1} corresponds to the stretching mode of ZnO bonds [39–41]. Absorption bands due to oxide and sulfate species are consistent with traces of zinc oxysulfate and zinc oxide impurities as characterized by XRD. All of these bands are disappeared by heat treatment at 600°C for 2 h in H_2S flow.

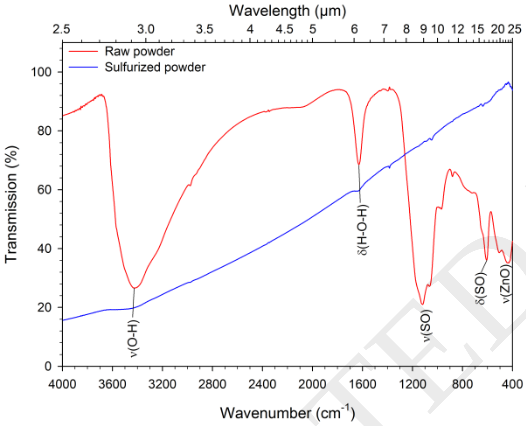

Fig. 2. FTIR-KBr spectra of ZnS raw and sulfurized powders

SEM images of raw and H_2S heat-treated powders are presented in Fig. 3. The combustion reaction produces porous structures which are easily hand-crushed into pale-yellow powders. The latter consist of large agglomerates with sizes up to 40 µm (details of one agglomerate are presented in Fig. 3a). The agglomerates are composed of particles of different size and shape, among which plate-like particles of sub-micrometric length and nanometric thickness and spherical nanometric particles. The specific surface area (SSA) of the as-combusted powders is about 13 m^2.g^{-1}.

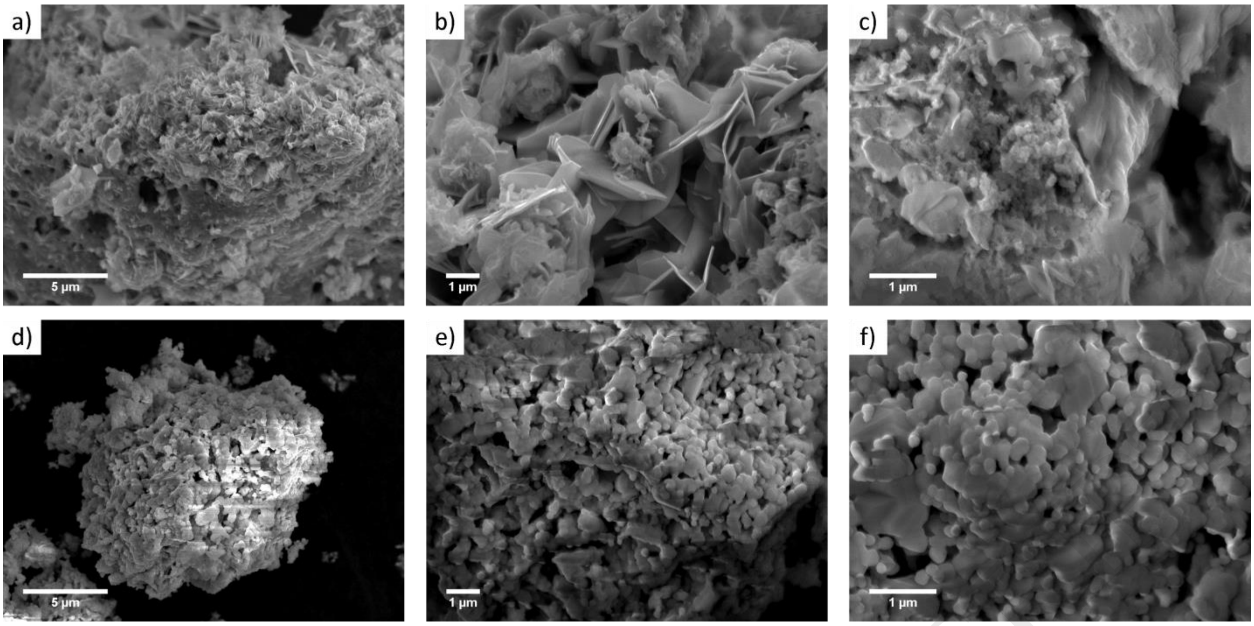

Fig. 3. SEM images of (a-c) raw powders and (d-f) sulfurized ZnS powders

After sulfurization, the morphology of the agglomerates is significantly modified. Primary particles have a more rounded shape and have grown to about 0.2-0.8 µm. At high magnification, SEM images show an interconnected microstructure produced by the partial sintering of the particles arising from the sulfurization heat treatment at 600°C. As a result, in comparison with the raw powders, the SSA of the pure powders is significantly reduced (3 $m^2.g^{-1}$).

The particle size distribution data of the pure ZnS powders represented in terms of a histogram and a cumulative size distribution are presented in Fig. 4. ZnS powders display a multi-modal particle size distribution, ranging from 0.1 to 40-50 µm. Four different populations can be identified in this broad granulometric distribution which is consistent with the SEM observations which show agglomerates of different sizes. The sub-micrometric population corresponds to the primary particles observed in SEM images (Fig. 3) with size centered on 0.5 µm.

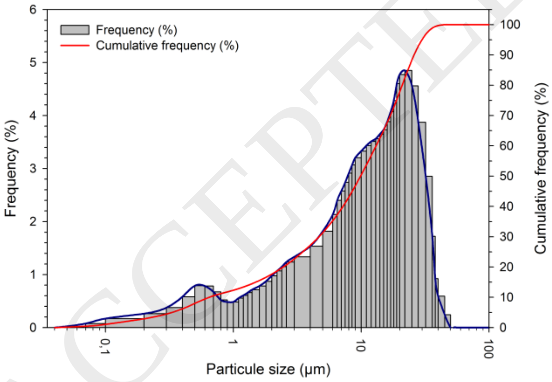

Fig. 4. Particle size and cumulative size distributions of ZnS powders

SEM-EDS analysis of the powders did not show any metallic impurity and Zn and S contents are in close agreement with the stoichiometric composition (50/50 at.%), considering the accuracy of EDS (~1 at.%).

TEM micrographs of raw powders are presented in Fig. 5 and Fig. 6. The morphology of the agglomerates is consistent with that observed by SEM where agglomerates appear to be made up of plate-like and spherical particles. Fig. 5c reveals that the plate-like particles consist of nanometric spherical grains.

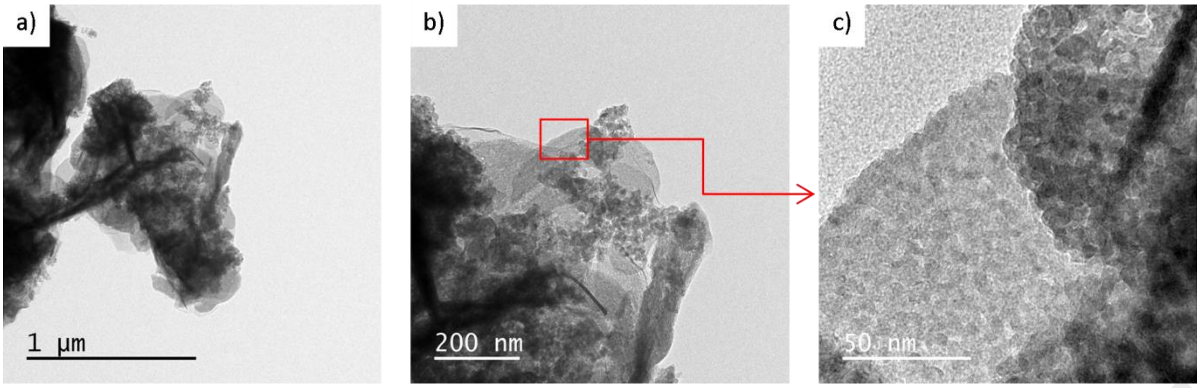

Fig. 5. Brightfield TEM micrographs of the ZnS raw powder

High magnification images of the raw powders (Fig. 6) show that the primary particles have a nanometric size (< 20 nm). In the inset of Fig. 6a, the Selected Area Electron Diffraction (SAED) pattern shows weak reflections (pointed by a "h") consistent with the coexistence of the hexagonal wurtzite 2H with the cubic sphalerite 3C. Note the wurtzite could not be evidenced on XRD patterns.

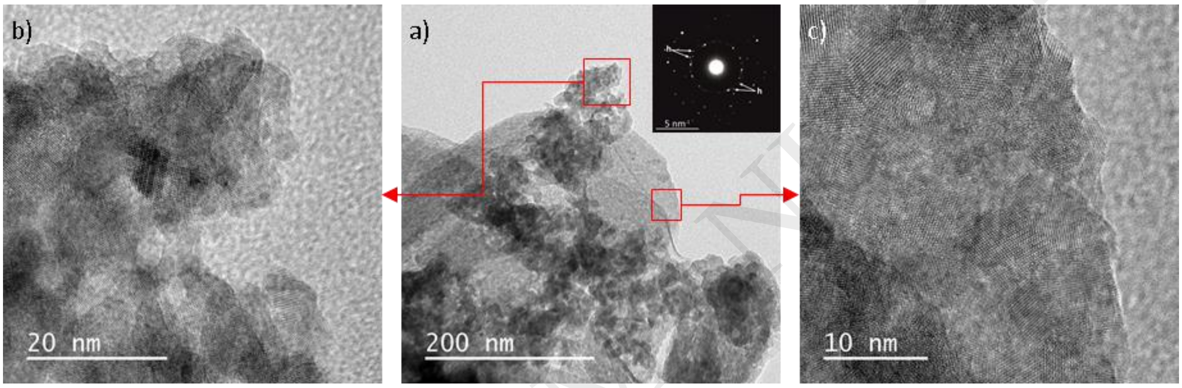

Fig. 6. (a) TEM micrograph of the ZnS raw powder. Inset: corresponding SAED pattern, "h" indicates reflections of the wurtzite 2H. High magnification micrographs of (b) agglomerates of spherical particles and (c) polycrystalline plate-like particles

TEM images of the sulfurized powders (Fig. 7) show agglomerates made up of nanometric particles of about 100-200 nm in size. As observed by SEM, these primary particles with rather spherical shape form agglomerates of 1 µm to few microns. High resolution images (Fig. 7c) of primary particles reveal the presence of planes defects normal to the [$\bar{1}$11] direction (labeled with a red arrow in Fig. 7c) of the sphalerite phase.

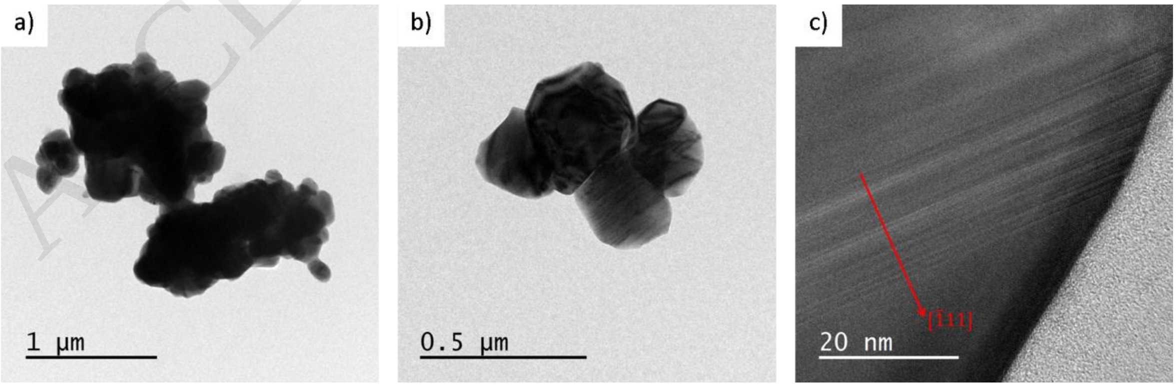

Fig. 7. Brightfield TEM micrographs of the ZnS sulfurized powder

Fig. 8a shows the SAED pattern of an oriented grain of a sulfurized powder along the [110] zone axis of the sphalerite lattice. The pattern exhibits bright reflections and diffuse lines. The main diffraction spots are consistent with the presence of twinned cubic sphalerite structure, the twinning plane being ($\bar{1}$11) (Fig. 8b&c). The weak reflections, marked by small arrows, correspond to the wurtzite 2H crystalline structure and result from local hexagonal stacking. The presence of the wurtzite phase and the twinning of the sphalerite phase are proofs of stacking faults along the cubic $[\bar{1}11]$ direction that could be described by a stacking sequence: ABCABACBA (twin, Fig. 9a) or ABCABABCA (simple stacking fault, Fig. 9b), where underlined stacking sequences correspond to layers of wurtzite involved in the fault. Disorder in this sequence direction due to random distribution of stacking faults is the cause of the diffusion lines. Note the strict notation should be AαBβCγ where the roman letters denote positions of layers of Zn atoms and the greek letters those of S atoms. The greek letters are omitted since the positions of the S atoms are fixed relative to the positions of the Zn atoms [42].

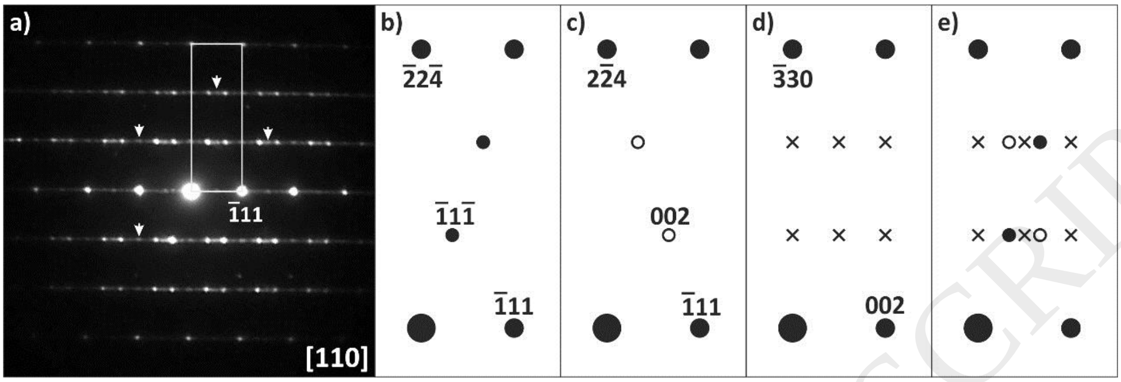

Fig. 8. (a) SAED pattern of a grain of the sulfurized powder along the [110] zone axis. The main reflections are attributed to the sphalerite crystalline structure with twinning and the arrows show some weak reflections of the wurtzite 2H crystalline structure. Simulations of reflection positions are drawn on (b) first twin of sphalerite, (c) second twin of sphalerite, (d) wurtzite and (e) superposition of all domains

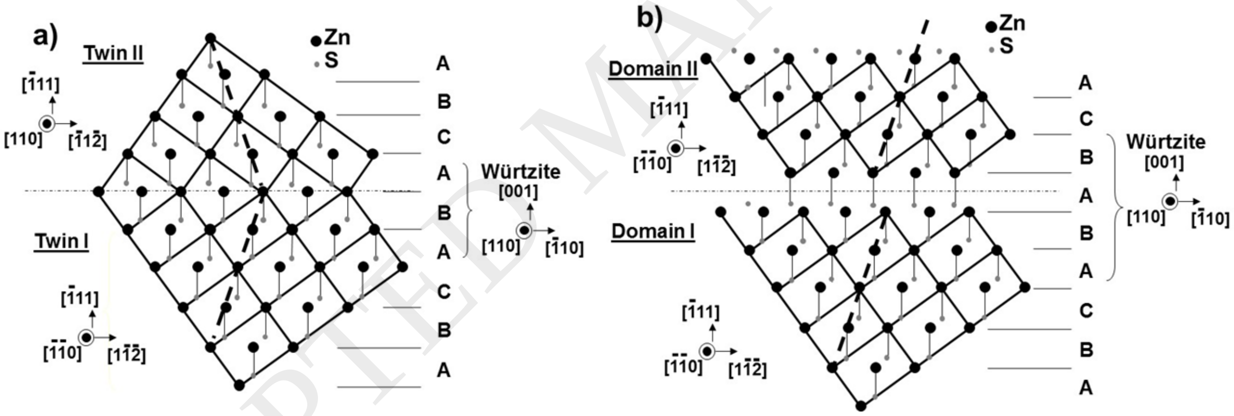

Fig. 9. Scheme of twinning (a) and of simple stacking fault (b) in the sphalerite ZnS leading to the formation of local hexagonal (3 and 4 wurtzite layers, respectively) sequence between cubic twinned crystals

4.2. Characterization of the ZnS ceramics

Table 1 reports the experimental sintering parameters, the relative density and photographs of the hot-pressed samples. The relative density obtained after a 2h dwell is of 99.4% while for 4h and 6h dwell it reaches > 99.9% which appears as the threshold for visible transparency. Full densification and transparent ceramics are thus obtained after a 4h dwell while the 2h-HP sample is white/pale-yellow translucent. Increasing the dwell time to 6 h leads to a higher densification by elimination of the residual porosity and, consequently, to a better transparency in the visible range.

Table 1. Sintering parameters, relative density and visual aspect of the hot-pressed ZnS ceramics

Sample	2h-HP	4h-HP	6h-HP

Temperature (°C)	950	950	950
Load (MPa)	120	120	120
Dwell time (h)	2	4	6
Densification	99.4%	>99.9%	>99.9%
Visual aspect (thickness = 1.5mm)			

The XRD patterns of the ZnS ceramics are displayed in Fig. 10. No drastic change is observed in the XRD patterns, compared to the initial powders. All diffraction patterns show the presence of the cubic sphalerite structure as the major phase and the hexagonal wurtzite 2H structure as a minor phase with the same relative proportion as in the powder (10-20% of hexagonal phase).

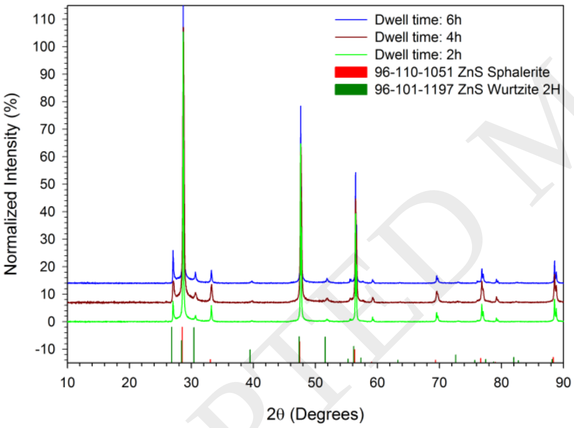

Fig. 10. XRD patterns of the hot-pressed ZnS ceramics

SEM micrographs and grain size distributions of thermally etched ceramic surfaces are presented in Fig. 11. All samples show a dense microstructure, with some residual pores localized at triple points (spotted by red arrows). As shown in Fig. 11c, the removal of almost all of the porosity has been achieved after a 6h dwell. The ceramics microstructure shows equiaxial grains, regular in shape. The grain sizes remain within a fairly narrow range, so the grain size distribution after a 6h dwell is fairly similar to that of a 2h dwell, with an average grain size centered on 1 µm. Interestingly, the grain size distribution after a 6h dwell is more unimodal giving rise to a more homogeneous microstructure.

SEM-EDS analysis of the ceramics did not show any impurity and Zn and S contents remain close to 50:50 regarding the accuracy of the method (± 1 at.%). Fortunately, the reducing conditions of hot pressing (vacuum and graphite environment) has no effect on the stoichiometry.

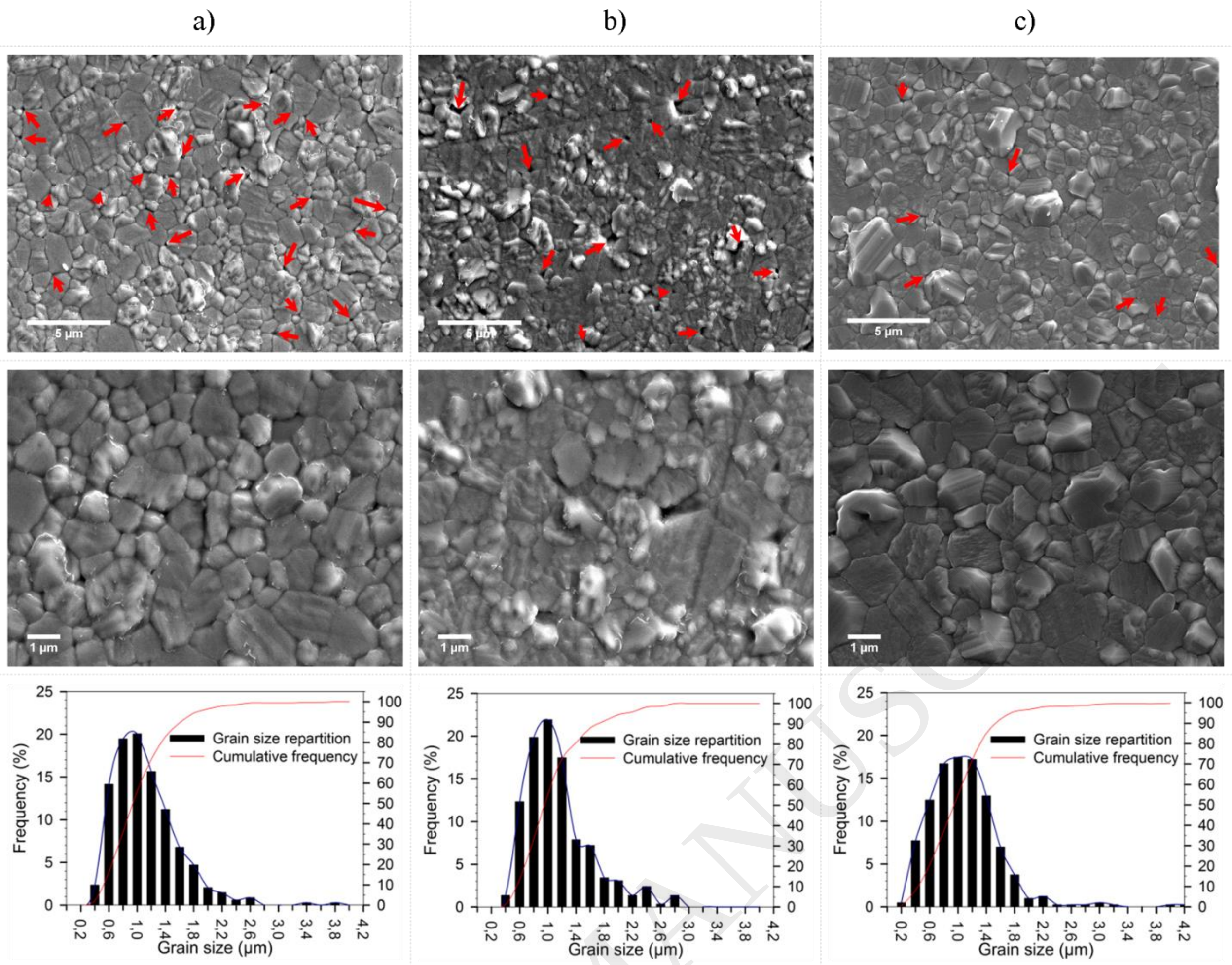

Fig. 11. SEM images of the thermally etched surfaces and grain size distribution of the ZnS ceramics hot-pressed at 950°C/120 MPa for (a) 2 h, (b) 4 h and (c) 6 h.

Fig. 12 shows the TEM images and the SAED patterns of an oriented ceramic grain along the [110] zone axis of the sphalerite lattice. As for the powder (Fig. 7), one can observe on the brightfield micrograph stacking faults oriented along the $(\bar{1}11)$ plane with a random distribution along the growth $[\bar{1}11]$ axis (Fig. 12a). The SAED pattern shows the presence of twinned sphalerite crystals, labeled with white arrows on the pattern (Fig. 12b). In some areas, weak reflections due to the wurtzite phase are also observed (Fig. 12c). The darkfield micrographs on Fig. 12d&e are built by selecting the 200 reflections of each sphalerite twin domain (labeled with white arrows on Fig. 12b). They show very inhomogeneous domains size (few nanometers to about 200 nm).

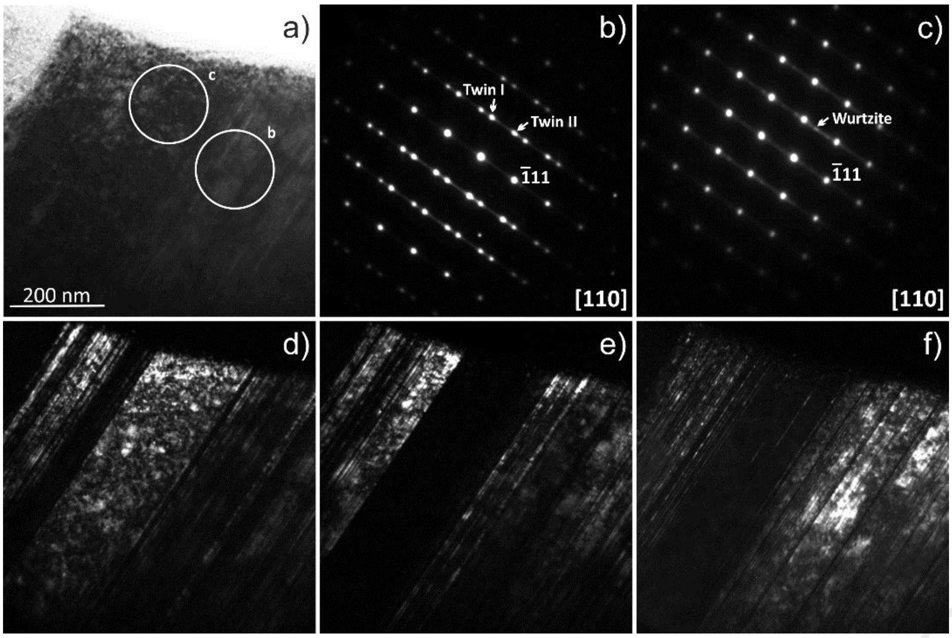

Fig. 12. Brightfield (a) and darkfield (d, e and f) TEM images of an oriented ZnS ceramic grain along the [110] zone axis. Diffraction patterns, shown in b) and c) respectively, correspond to area spotted in a). Arrows show the reflections used for the images.

Fig. 12f presents a darkfield image built from the 100 reflections of the wurtzite phase (labeled with a white arrow on Fig. 12c). This reflection is weak and superimposed with a diffuse line. As a result, the contrast is weak and a small contribution of the cubic phase is probably present, nevertheless one can see fine bright lines in the large cubic domains in the center of the image. These lines correspond to wurtzite phase domains. Each interphase between domains is a stacking fault. On both SAED patterns, diffuse lines contributions are present along $(\bar{1}11)$ planes that are due to the random distribution of the numerous twin faults, that lead to structural departures of the ideal crystalline lattice along the $[\bar{1}11]$ direction, known to give rise to diffuse effects [42]. The high resolution image, shown in Fig. 13, registered in the area labeled "b" in Fig. 12a displays a high density of twin defaults in agreement with the results displayed in Fig. 12. This figure shows that the domains could be as small as one or two wurtzite unit cells thick and that these important deviations of the ideal structure is at the origin of the diffusive unidimensional effect observed in Fig. 12. This image displays twins, that involve a change of the sequence direction, as schemed in Fig. 9a, and simple stacking faults that do not involve such change, as in Fig. 9b. Since these results are similar to that obtained on powders, the sintering process has no influence on the presence, the number and the distribution of the stacking faults (i.e. cubic and hexagonal domains).

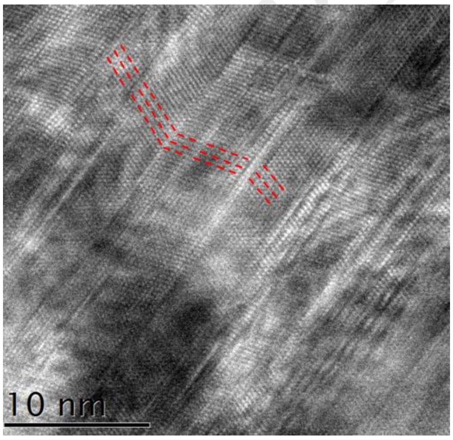

Fig. 13. High resolution image registered in the area labeled "b" on Fig. 12a. Red dashed lines have been added to aid the eye in identifying twins and simple stacking faults.

Fig. 14 shows micrographs of grain boundaries in densified zinc sulfide. No secondary nor non-crystalline phase was found at the interface. High resolution micrographs (Fig. 14b'&c') show regular stackings of atomic planes of the oriented grain with steps formation at the grain boundary to match the stacking orientation of the neighboring grain.

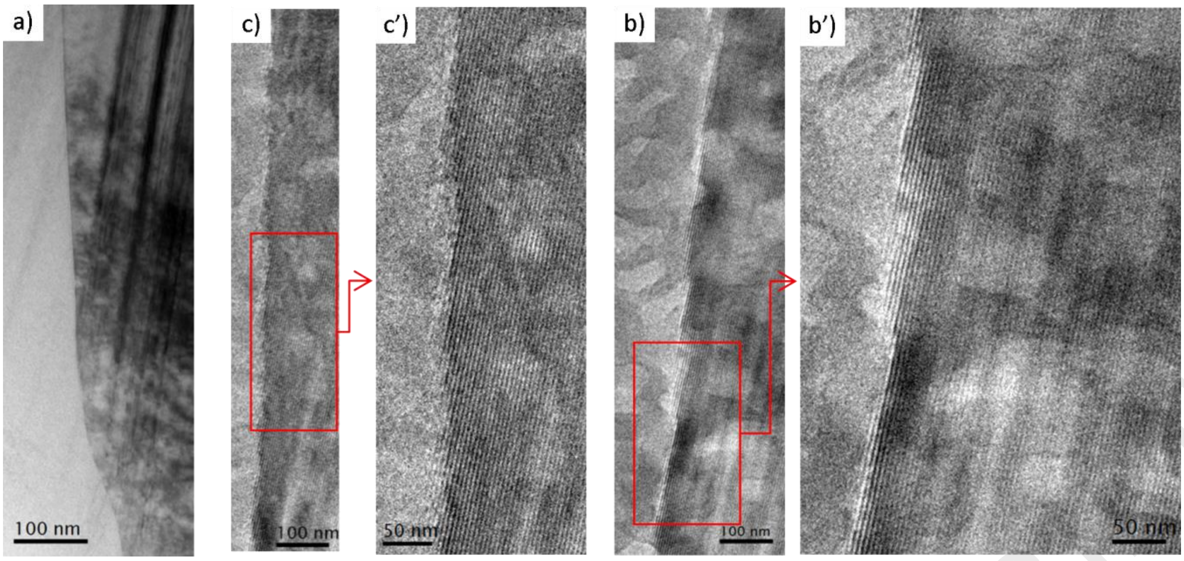

Fig. 14. Brightfield TEM micrographs of grain boundary at a) low resolution/magnification and b) and c) high resolution/magnification

4.3. Optical transmission of the ceramics

The transmission spectra were recorded between 2.5 and 16 µm at room temperature on the polished 1.5 mm-thick samples presented in Table 1 (Fig. 15).

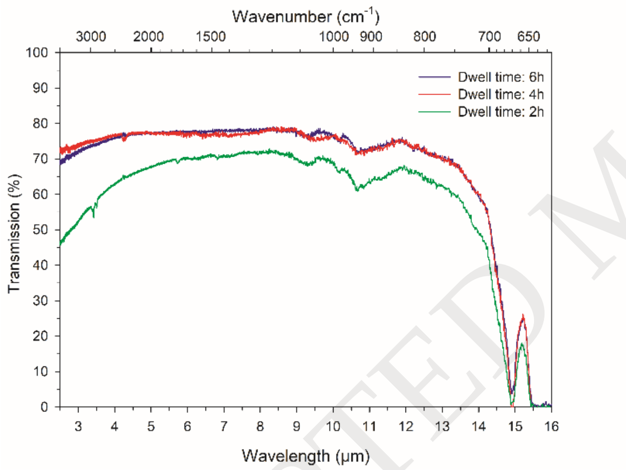

Fig. 15. Infrared transmission of the hot-pressed ZnS ceramics (thickness = 1.5mm)

The three samples exhibit a high transmission level. Variation in the transmission level is however observed for the 2h-HP sample which offers a lower transmission of at least about 5% in the full range. This result is in agreement with its lower densification (99.4%). The transmission spectra of 4h-HP and 6h-HP samples with >99.9% densification each are logically overlapping reaching the theoretical level of 75% in the range 4-12 µm. The increase in transmission correlates to the densification rate which increases with sintering time. Transmission loss due to scattering phenomena is observed for all samples at low wavelengths (<5 µm). Let us note that in the absence of suitable technique to access porosity of less than 0.1%, which is beyond the accuracy of the used density measurement, we assume that increasing the sintering time helps to remove more porosity and tiny voids and thus contributes to the scattering decrease.

The transmission spectra present absorption bands at 9 µm and 10-11 µm. These bands are respectively attributed to the vibration of SO_4^{2-} [1] and SO_3^{2-} groups [3] which originate from adsorbed oxygenated species after powders exposure to ambient air.

5. Discussion

5.1. Powders synthesis and sulfurization

The combustion synthesis using high purity zinc nitrate and TAA produces ZnS precursors that are easily converted in pure ZnS by a heat treatment in H_2S. ZnS powders are composed of agglomerates made of “pre-sintered” nanometric particles with size centered on 0.5 µm. The effectiveness of the synthesis method is based on the speed of the combustion reaction which confers to the raw powder a rather large SSA for subsequent gaseous treatment. The nanometric particles are thus purified within 2 h in an H_2S flow at 600°C. The exposure time and temperature are respectively sufficiently short and low to retain particles of sub-micrometric size so as to ensure high sinterability.

TEM characterizations show that powders crystallize as cubic sphalerite ZnS with twins or simple stacking faults leading to the formation of local hexagonal sequences between cubic twinned crystals. As identified by SAED, the hexagonal domains form readily in the raw powder. If some isolated grains show pure or almost pure sphalerite structure, without twins, no pure wurtzite grains were found by TEM. Therefore, assumption can be made that wurtzite 2H secondary phase, detected by XRD, is due to the numerous local hexagonal sequences randomly generated by the stacking faults in the cubic phase. So, the proportion of hexagonal phase (10-20%), calculated by comparison of the wurtzite (100) and sphalerite (111) peak integrated intensities, should be considered more like a percentage of structural local disorder rather than a proportion of secondary phase. Microtwinning is already reported to lead to “false hexagonality” in X-ray diffraction studies [43].

In addition, TEM observation of stacking faults highlights the diffuse baseline in the 2θ range 26-34° in the XRD patterns (inset of Fig. 1b). The random distribution of the stacking faults induces diffusion lines in SAED patterns and a diffuse halo in XRD patterns (no surstructure peaks). Moreover, due to the anisotropy of the diffracting domains, the latter is dependent on the stacking direction ($[\bar{1}11]$ for sphalerite and [001] for wurtzite) with large peaks for high contribution in the stacking direction due to domain size of few angströms to several nanometers and thin peaks for contribution perpendicular to the stacking direction due to large domain size (about the grain size, from 0.5 to 2µm).

5.2. Ceramic densification and optical properties

Sintering conditions for high densification have been reached using hot pressing at 950°C under 120 MPa. Despite an apparent unfavorable morphology (Fig. 3), particles sinter to reach the theoretical density after only 4h-hot pressing. The grain size distribution in the ceramics is radically different to that of the powders giving rise to a unimodal distribution centered on 1 µm. This indicates the agglomerates are soft enough to collapse during sintering to finally produce an homogeneous microstructure. In addition, the SEM micrographs and grain size distribution point out a normal grain growth during hot pressing resulting in fairly similar grain size distributions. From Fig. 11b&c it can be seen that prolonged sintering time tends to narrow the grain size distribution, with at least 80% of sizes between 0.4 and 1.6 µm. This microstructure evolution is enabled by pores lying exclusively at triple points outside the grains (Fig. 11) making them easy to remove to achieve full densification. We assume the separation of the grain boundaries from the pores is prevented through the rather moderate sintering temperature.

High dense (>99.9%) ceramics have a transmission of the theoretical level (75%) in the range 4-12µm. The optical loss at low wavelengths can not be attributed to absorption phenomena (high purity samples if we except the “S-O” chemisorbed surface groups) but to scattering. Residual porosity, as attested by SEM observations, is easily eliminated and/or significantly reduced after hot pressing for 6 h so that the optical performances, in the 2.5-16µm range, are comparable to that of a colorless multispectral CVD ZnS (Cleartran®).

TEM characterization shows comparable results for ceramics and powders. Wurtzite phase domains form from the first step of the synthesis process and the sintering conditions do not allow the transformation from hexagonal to cubic stacking. The hexagonal domains by creating birefringence also contribute to the transmission loss in the visible. Nevertheless, due to the size of these diffusion domains and to the low refractive-index mismatch between sphalerite and wurtzite, the contribution of the hexagonal phase to the diffusion is weak compared to that of the residual porosity, particularly in the near infrared. Post-HIP treatment would allow the removal of the residual porosity, and as for CVD ZnS, would transform the hexagonal domains into cubic phase.

It is interesting to mention that small amounts of hexagonal phase is also typical of ZnS crystals grown from the melt (Bridgman technique) or polycristalline ZnS CVD [25]. The occurence of hexagonal domains in ZnS is not specific of the fabrication process but is a consequence of a very low twinning stacking-fault energy (estimated <6 $mJ.m^{-2}$) [44].

In previous work [13], we emphasized the detrimental consequences of insufficient control of the powder quality such as the particle size, the state of agglomeration, the purity, in the development of the microstructure and the subsequent optical properties. The most profound effect of the particle size and state of agglomeration is on the sintering. The powder synthesis procedure is thus of prime importance to produce the desired microstructure. Compared to ceramics elaborated from precipitated powders [13,15,21], significant progress has been realized with combusted powders in terms of visual aspect and optical properties which reach the theoretical level of about 75% in the 4-12 µm region. To the best of our knowledge, we report unprecedented optical performances (at equivalent thickness) for hot-pressed ZnS ceramics.

Finally, one additional consideration in our ceramics is the occurrence of SO_4^{2-} and SO_3^{2-} species which absorb strongly in the 8-14 μm atmospheric window. We managed to maintain the oxygen content as low as possible to ensure an optimized transmission. Removal of the residual oxygen is always one of the most critical processing steps to achieve excellent transmission and make ZnS useful infrared window.

6. Conclusion

Transparent ZnS ceramics were obtained through hot pressing of high purity powders synthesized by a newly developed combustion method. The optimum sintering conditions produce transparent ceramics performing better than standard grade CVD ZnS with transmission near if not identical to Multispectral CVD ZnS in the 4-12 μm range. TEM characterizations bring new insights on the local structure of ZnS powders and ceramics with the identification of the nature of stacking defaults and its correlation to the optical properties. Optical performances have been explained in terms of scattering effects induced by porosity and birefringence created by the stacking faults which considerably affect the transmission in the visible. As for CVD ZnS, optical quality of the hot-pressed ceramics could be further improved by post-HIP treatment. One exciting development of these transparent ceramics is expected in the area of active optics.

Acknowledgements

SEM and TEM experiments were performed on CMEBA and THEMIS platforms, respectively (ScanMAT, UMS 2011 University of Rennes 1-CNRS; CPER-FEDER 2007–2014).

7. References

[1] E. Khawaja, S.G. Tomlin, The optical constants of thin evaporated films of cadmium and zinc sulphides, J. Phys. Appl. Phys. 8 (1975) 581. doi:10.1088/0022-3727/8/5/019.

[2] J.R. Bakke, J.S. King, H.J. Jung, R. Sinclair, S.F. Bent, Atomic layer deposition of ZnS via in situ production of H_2, Thin Solid Films. 518 (2010) 5400–5408. doi:10.1016/j.tsf.2010.03.074.

[3] O.L. Arenas, M.T.S. Nair, P.K. Nair, Chemical bath deposition of ZnS thin films and modification by air annealing, Semicond. Sci. Technol. 12 (1997) 1323. doi:10.1088/0268-1242/12/10/022.

[4] S.R. Steele, J. Pappis, Chemical Vapor Deposition of IR Materials, Raytheon Company, Reseasch Division, 1973. http://www.dtic.mil/dtic/tr/fulltext/u2/887137.pdf (accessed April 21, 2016).

[5] D.C. Harris, Durable 3–5 μm transmitting infrared window materials, Infrared Phys. Technol. 39 (1998) 185–201. doi:10.1016/S1350-4495(98)00006-1.

[6] D.C. Harris, Development of hot-pressed and chemical-vapor-deposited zinc sulfide and zinc selenide in the United States for optical windows, in: R.W. Tustison (Ed.), Proceedings of SPIE, 2007: pp. 654502-654502–27. doi:10.1117/12.716808.

[7] S.S. Singh, S. Pratap, J. Prasad, R. Kumar, K. Murari, Infrared (8-12 um) Dome Materials: Current Status, Def. Sci. J. 48 (1998) 173–183. doi:10.14429/dsj.48.3897.

[8] D.C. Harris, M. Baronowski, L. Henneman, L. LaCroix, C. Wilson, S. Kurzius, B. Burns, K. Kitagawa, J. Gembarovic, S.M. Goodrich, C. Staats, J. Mecholsky John J., Thermal, structural, and optical properties of Cleartran® multispectral zinc sulfide, Opt. Eng. 47 (2008) 114001-114001–15. doi:10.1117/1.3006123.

[9] J.E. Carnall, P.B. Mauer, W.F. Parsons, D.W. Roy, Zinc sulfide optical element, US Patent 3,131,025, 1964.

[10] E. Carnall, Hot-Pressing of ZnS and CdTe, J. Am. Ceram. Soc. 55 (1972) 582–583. doi:10.1111/j.1151-2916.1972.tb13444.x.

[11] M. Hasegawa, Optical characteristics of an infrared translucent close packed ZnS sintered body, SEI Tech. Rev. 54 (2002) 12-13+71.

[12] Y. Li, Y. Wu, Transparent and Luminescent ZnS Ceramics Consolidated by Vacuum Hot Pressing Method, J. Am. Ceram. Soc. 98 (2015) 2972–2975. doi:10.1111/jace.13781.

[13] C. Chlique, O. Merdrignac-Conanec, N. Hakmeh, X. Zhang, J.-L. Adam, Transparent ZnS Ceramics by Sintering of High Purity Monodisperse Nanopowders, J. Am. Ceram. Soc. 96 (2013) 3070–3074. doi:10.1111/jace.12570.

[14] C. Li, T. Xie, J. Dai, H. Kou, Y. Pan, J. Li, Hot-pressing of zinc sulfide infrared transparent ceramics from nanopowders synthesized by the solvothermal method, Ceram. Int. 44 (2018) 747–752. doi:10.1016/j.ceramint.2017.09.242.

[15] Christophe Chlique, Préparation et caractérisation de poudres et céramiques (oxy) sulfures pour applications en optique active et passive, Thèse de l'Université Rennes 1, 2011. http://hal.archives-ouvertes.fr/tel-00678255/.

[16] Noha Hakmeh, Élaboration et caractérisation de luminophores céramiques optiques IR à base d'(oxy)sulfures, Thèse de l'Université de Rennes 1, 2014.

[17] K.-T. Lee, B.-H. Choi, J.-U. Woo, J.-S. Kang, J.-H. Paik, B.-U. Chu, S. Nahm, Microstructural and optical properties of the ZnS ceramics sintered by vacuum hot-pressing using hydrothermally synthesized ZnS powders, J. Eur. Ceram. Soc. 38 (2018) 4237–4244. doi:10.1016/j.jeurceramsoc.2018.05.018.

[18] C. Li, Y. Pan, H. Kou, H. Chen, W. Wang, T. Xie, J. Li, Densification Behavior, Phase Transition, and Preferred Orientation of Hot-Pressed ZnS Ceramics from Precipitated Nanopowders, J. Am. Ceram. Soc. 99 (2016) 3060–3066. doi:10.1111/jace.14334.

[19] C. Li, T. Xie, H. Kou, Y. Pan, J. Li, Hot-pressing and post-HIP treatment of Fe^{2+}:ZnS transparent ceramics from co-precipitated powders, J. Eur. Ceram. Soc. 37 (2017) 2253–2257. doi:10.1016/j.jeurceramsoc.2016.12.051.

[20] S.-Y. Yeo, T.-H. Kwon, C.-S. Park, C.-I. Kim, J.-S. Yun, Y.-H. Jeong, Y.-W. Hong, J.-H. Cho, J.-H. Paik, Sintering and optical properties of transparent ZnS ceramics by pre-heating treatment temperature, J. Electroceramics. 41 (2018) 1–8. doi:10.1007/s10832-018-0137-y.

[21] C. Chlique, G. Delaizir, O. Merdrignac-Conanec, C. Roucau, M. Dollé, P. Rozier, V. Bouquet, X. Zhang, A comparative study of ZnS powders sintering by Hot Uniaxial Pressing (HUP) and Spark Plasma Sintering (SPS), Opt. Mater. 33 (2011) 706–712. doi:10.1016/j.optmat.2010.10.008.

[22] Y. Chen, L. Zhang, J. Zhang, P. Liu, T. Zhou, H. Zhang, D. Gong, D. Tang, D. Shen, Fabrication of transparent ZnS ceramic by optimizing the heating rate in spark plasma sintering process, Opt. Mater. (2015). doi:10.1016/j.optmat.2015.03.058.

[23] Y. Li, L. Zhang, K. Kisslinger, Y. Wu, Green phosphorescence of zinc sulfide optical ceramics, Opt. Mater. Express. 4 (2014) 1140–1150. doi:10.1364/OME.4.001140.

[24] H.-Y. Ahn, W.J. Choi, S.Y. Lee, B.-K. Ju, S.-H. Cho, Mechanochemical synthesis of ZnS for fabrication of transparent ceramics, Res. Chem. Intermed. 44 (2018) 4721–4731. doi:10.1007/s11164-018-3277-4.

[25] J.S. McCloy, Properties and processing of chemical vapor deposited zinc sulfide, PhD dissertation of the University of Arizona, 2008. http://www.academia.edu/download/41742633/Properties_and_processing_of_chemical_va20160129-20495-3jkug.pdf (accessed November 2, 2015).

[26] P. Ramavath, V. Mahender, U.S. Hareesh, R. Johnson, S. Kumari, N. Eswara Prasad, Fracture behaviour of chemical vapour deposited and hot isostatically pressed zinc sulphide ceramics, Mater. Sci. Eng. A. 528 (2011) 5030–5035. doi:10.1016/j.msea.2011.03.031.

[27] C.S. Chang, J.L. He, Z.P. Lin, The grain size effect on the empirically determined erosion resistance of CVD-ZnS, Wear. 255 (2003) 115–120. doi:10.1016/S0043-1648(03)00266-7.

[28] D. Townsend, J.E. Field, Fracture toughness and hardness of zinc sulphide as a function of grain size, J. Mater. Sci. 25 (1990) 1347–1352. doi:10.1007/BF00585448.

[29] A.F. Shchurov, E.M. Gavrishchuk, V.B. Ikonnikov, E.V. Yashina, A.N. Sysoev, D.N. Shevarenkov, Effect of Hot Isostatic Pressing on the Elastic and Optical Properties of Polycrystalline CVD ZnS, Inorg. Mater. 40 (2004) 336–339. doi:10.1023/B:INMA.0000023950.21533.78.

[30] N. Hakmeh, O. Merdrignac-Conanec, X. Zhang, Method of manufacturing a sulfide-based ceramic element particularly for IR-optics applications, EP 2 966 051 A1, 2016. https://patents.google.com/patent/US20170144934A1/fr.

[31] T. Bansagi, E.A. Secco, O.K. Srivastava, R.R. Martin, Kinetics of hexagonal–cubic phase transformation of zinc sulfide in vacuo, in zinc vapor, and in sulfur vapor, Can. J. Chem. 46 (1968) 2881–2886. doi:10.1139/v68-479.

[32] L.A. Xue, R. Raj, Superplastic Deformation of Zinc Sulfide Near Its Transformation Temperature (1020°C), J. Am. Ceram. Soc. 72 (1989) 1792–1796. doi:10.1111/j.1151-2916.1989.tb05980.x.

[33] H.H. Li, Refractive Index of ZnS, ZnSe, and ZnTe and Its Wavelength and Temperature Derivatives, J. Phys. Chem. Ref. Data. 13 (1984) 103–150. doi:10.1063/1.555705.

[34] A. Janca, K. Tereszchuk, P.F. Bernath, N.F. Zobov, S.V. Shirin, O.L. Polyansky, J. Tennyson, Emission spectrum of hot HDO below 4000 cm^{-1}, J. Mol. Spectrosc. 219 (2003) 132–135. doi:10.1016/S0022-2852(03)00015-8.

[35] R. Lemus, Vibrational excitations in H_2O in the framework of a local model, J. Mol. Spectrosc. 225 (2004) 73–92. doi:10.1016/j.jms.2004.02.015.

[36] D.A. Panayotov, J.T. Yates Jr., Depletion of conduction band electrons in TiO_2 by water chemisorption – IR spectroscopic studies of the independence of Ti–OH frequencies on electron concentration, Chem. Phys. Lett. 410 (2005) 11–17. doi:10.1016/j.cplett.2005.03.146.

[37] F. Babou, G. Coudurier, J.C. Vedrine, Acidic Properties of Sulfated Zirconia: An Infrared Spectroscopic Study, J. Catal. 152 (1995) 341–349. doi:10.1006/jcat.1995.1088.

[38] H. Böke, S. Akkurt, S. Özdemir, E.H. Göktürk, E.N. Caner Saltik, Quantification of $CaCO_3$–$CaSO_3 \cdot 0{,}5H_2O$–$CaSO_4 \cdot 2H_2O$ mixtures by FTIR analysis and its ANN model, Mater. Lett. 58 (2004) 723–726. doi:10.1016/j.matlet.2003.07.008.

[39] N.T. McDevitt, W.L. Baun, Infrared absorption study of metal oxides in the low frequency region (700-240 cm^{-1}), Spectrochim. Acta. 20 (1964) 799–808. doi:10.1016/0371-1951(64)80079-5.

[40] S. Maensiri, P. Laokul, V. Promarak, Synthesis and optical properties of nanocrystalline ZnO powders by a simple method using zinc acetate dihydrate and poly(vinyl pyrrolidone), J. Cryst. Growth. 289 (2006) 102–106. doi:10.1016/j.jcrysgro.2005.10.145.

[41] A. Kajbafvala, S. Zanganeh, E. Kajbafvala, H.R. Zargar, M.R. Bayati, S.K. Sadrnezhaad, Microwave-assisted synthesis of narcis-like zinc oxide nanostructures, J. Alloys Compd. 497 (2010) 325–329. doi:10.1016/j.jallcom.2010.03.057.

[42] M.T. Sebastian, P. Krishna, Single crystal diffraction studies of stacking faults in close-packed structures, Prog. Cryst. Growth Charact. 14 (1987) 103–183. doi:10.1016/0146-3535(87)90017-7.

[43] M.P. Kulakov, S.Z. Shmurak, Structural changes in ZnS crystals on account of partial dislocation movement, Phys. Status Solidi A. 59 (1980) 147–153. doi:10.1002/pssa.2210590120.

[44] S. Takeuchi, K. Suzuki, K. Maeda, H. Iwanaga, Stacking-fault energy of II–VI compounds, Philos. Mag. A. 50 (1985) 171–178. doi:10.1080/01418618408244220.